

# An approach integrating BIM, octree and FEM-SBFEM for highly efficient modeling and seismic damage analysis of building structures

Degao Zou<sup>a,b</sup>, Kai Chen<sup>a,b,\*</sup>, Xianjing Kong<sup>a,b</sup>, Xiang Yu<sup>a,b,\*</sup>

<sup>a</sup> The State Key Laboratory of Coastal and Offshore Engineering, Dalian University of Technology, Dalian, Liaoning 116024, China

<sup>b</sup> School of Hydraulic Engineering, Dalian University of Technology, Dalian, Liaoning 116024, China

## ARTICLE INFO

### Keywords:

Octree  
SBFEM  
Building information modeling  
Detailed grids  
Structure damage

## ABSTRACT

This paper presents a novel BIM-Octree-FEM-SBFEM method (BOFSM) for rapid modeling and seismic damage analysis of structures. The BOFSM enables rapid and accurate modeling of structures by incorporating three innovative improvements. Firstly, integrating the digital building information method (BIM) with the Octree algorithm for discretization, a complex geometric model can be directly transformed into an analysis model. The automated transformation process eliminates considerable manual efforts typically expended in the traditional method. Secondly, the solver is improved using finite element method (FEM) to solve the hexahedrons elements while using scaled boundary FEM (SBFEM) to solve the polyhedrons. Thirdly, a nonlinear similar element (NSE) technique is proposed for cubes that occupy about 80% of the meshes. The matrices of one unit cubic element are pre-computed and stored in memory. Subsequently, the parameters of each element can be directly computed by scaling the dimensional coefficient and damage factor, thus offering an economical computational approach for massive matrices in damage analyses. The above methods are implemented in an in-house program GEODYNA, with CPU+GPU parallelization and multitasking capacity. Two refined seismic destruction analyses for frame buildings were conducted and some potential advantages are discussed. The results demonstrate the efficiency, universality and robustness of the BOFSM.

## 1. Introduction

The Finite Element Analysis (FEA) of structures typically involves the following four procedures: (1) the construction of a geometric model, (2) discretization, (3) numerical analysis and (4) post-processing. In the first procedure, the most common approach is to build the 3D geometric model starting from the basic elements (i.e. bottom-up approach). Each elements (points, line and area) are created one after another, according to the given design schematics. Correspondingly, there is also an up-bottom modeling method, which builds the body first, and then automatically generates the surfaces, lines and points, which is suitable for general geometry (i.e. cylinder, cuboid, sphere, etc.). In addition to the painstaking and time consuming process of the bottom-up approach, we must also consider the iterative efforts taken by structural engineers to come up with a feasible design. This entire process of building the model is estimated to take over 57% of overall analysis time [1]. This situation is a strong motivator to develop an innovative pre-processing program that enables efficient modeling and fast, automatic discretization and solution techniques.

In regards to the above problem, an emerging technique, called Building Information Modeling (BIM), can serve as a powerful solution. BIM has even been hailed as the marker of a second technological revolution in engineering structure design [2]. This technology has taken over as the new computer aided design (CAD) paradigm increasingly in architecture, engineering, and construction (AEC) for both industrial and academic circles [2]. BIM benefits the structural design process by enabling systematic modeling functions, interactive visualization, and standardised data exchange interfaces [3]. While the advancement of computational technologies makes the modeling process easier than ever before, the above-mentioned benefits of BIM are rarely realized in FEA to a lack of integration among modeling, discretization and solution modules within FEA software. For now, the main application of BIM is geometric representation, work planning, construction and operation. In order to make full use of the advantages of BIM, it is necessary to explore new discrete methods and solution techniques.

For the second procedure (discretization), the octree algorithm is often used due to its highly efficient meshing methods as well as robust grid adaptation, rapid mesh regeneration and straightforward data

\* Corresponding authors at: The State Key Laboratory of Coastal and Offshore Engineering, Dalian University of Technology, Dalian, Liaoning 116024, China.  
E-mail addresses: [chenkai@mail.dlut.edu.cn](mailto:chenkai@mail.dlut.edu.cn) (K. Chen), [xiangyu@mail.dlut.edu.cn](mailto:xiangyu@mail.dlut.edu.cn) (X. Yu).

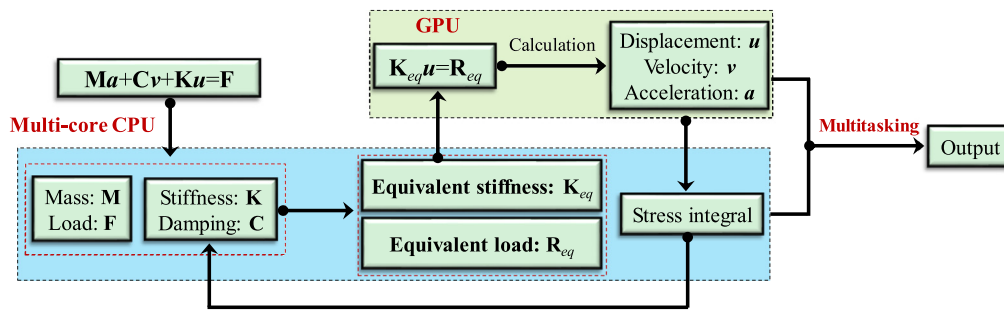


Fig. 1-1. Illustration of hanging node in grids generated from Octree algorithm.

access. Such advantages are made possible due to the use of simple Cartesian structure and embedded hierarchy [4]. The octree algorithm enjoys an increasing usage in the numerical computing community for applications in computational fluid dynamics, plasma physics and other fields [4–7]. However, the algorithm generates extra hanging nodes on partial edges [8–10], which will lead to uneven displacement on adjacent edges (shown in Fig. 1-1). On the other hand, the use of polyhedron elements would be an effective solution for the problem; the Scaled Boundary FEM (SBFEM), recently developed by Wolf and Song [11], implements such a solution and is used in this study.

One advantage of SBFEM is that only the boundary discretization is required, similar to the boundary element method (BEM) [12,13], and the fundamental solution is not required. A second advantage of SBFEM is the flexibility and versatility inherited from FEM. The third advantage is that this method is semi-analytical, wherein the linear element has high accuracy compared to FEM. After two decades of development, many researchers have made efforts to focus on expanding the application and improving SBFEM. Liu et al. [14,15] analysed electromagnetic problems using SBFEM, and a good performance was demonstrated. Ooi et al. [16] then improved the method to perform nonlinear analysis. Subsequently, Chen et al. [17,18] formulated more convenient and practical elasto-plastic solutions for 2D and 3D problems, and expanded the application of SBFEM to geotechnical problems. As stress singularities can be solved perfectly via SBFEM, multiple researchers have used the method in crack propagation problems [19–22]. Lu et al. [23] and Birk and Behnke [24] modified the SBFEM for the problems regarding layered soil and soil-structure interactions. Furthermore, SBFEM based modeling of 3D steady-state heat conduction in anisotropic layered media was developed in [25]. Lin et al. [26] applied this SBFEM for sloshing analysis of liquid storage tanks. A nonlinear analysis of dynamic interactions of CFRD-compressible reservoir system was introduced by Xu et al. [27]. Use of SBFEM in wave interaction and propagation simulations were reported in [28–30]. Other applications include heat conduction problems [31], computation of hydrodynamic pressure in seismic problems [32,33], nonlinear dynamic liquefaction analysis of saturated soil [34], and rapid automatic image-based stress analysis [9,10]. More recently, some research findings have been published, such as a novel error indicator and an adaptive refinement technique are discussed [35], application of arbitrary faceted star convex polyhedral [36], elasto-dynamics analysis has been conducted [37], mesoscale fracture modeling in concrete using SBFEM [38], simulation of crack propagation modeling in functionally graded materials [39], stress analysis of 3D complex geometries [40], Saputra and coworkers reported the computation of three-dimensional fracture parameters [41], and Zhang et al. conducted damage evolution analysis [42,43]. A global concurrent cross-scale nonlinear analysis approach (GCCNA) that is based on SBFEM was published [44]. GCCNA is attractive for practical applications due to potential for efficient refinement analysis of large, complex engineering structures.

In summary, we have three parallel developments (BIM technology for modeling complex 3D architectures, octree generator for discretization, and elasto-plastic polyhedron SBFEM for numerical computation),

we can now aim to improve the process for analysing the evolution of seismic damage on engineering structures. The feedback enabled by the above developments will help increase the integrity and security of key civil infrastructure.

The objective of this paper is to synthesize an innovative combination of BIM and an efficient octree-based mesh, as will be shown in Section 2. In Section 3, we will introduce a simple SBFEM approach for polyhedron formulation and developing the model for concrete damage plasticity. The verification and practicality of the procedures is discussed in Section 4. Finally, remarks and conclusions about the method are summarized in Section 5.

## 2. Integrating BIM and structural analysis

### 2.1. CAD-to-CAE-to-FEM (traditional: repetitive manual efforts, cumbersome and error-prone)

There are two kinds of methods of analysing engineering structures: wire-frame analysis with the bar and shell elements; and the other is through solid elements. As shown in Fig. 2-1, in wire-frame analysis, it is easy to use and can quickly understand the overall response of the structure, while the method is difficult to capture structural damage and destruction. Thus in this paper, we focus on the use of solid elements for FEM modeling.

Establishing the solid model is the first step in finite element analysis, and the model is the key to decide whether the analysis result is reasonable or not. Traditionally, space structures are designed from a bottom-up approach. Thus geometric elements such as points, lines and surfaces are created one after another. All elements are subsequently combined to generate the whole geometric model (see Fig. 2-1). Considerable manual effort is needed from the engineer to construct the model, which makes the pre-processing cumbersome and error-prone. Since the engineer is not actually changing the original design of the structure in this step, most of the work at this stage is repetitive work. The more complex the structure is, the more difficult it is to completely match the digital model to the original schematics. It is estimated that creation of an analysis-suitable geometry requires about 57% of overall analysis time [1]. Therefore, the modeling process has much potential for improvement in terms of efficiency and accuracy.

### 2.2. BIM-to-bar-shell element analysis (difficult to capture failure processes)

As a newly developed 3D structure design method, BIM is a generalized terminology that encompasses the integration of advanced methods for a complete digital representation of a building's geometry, performance, planning, construction and operation [45]. BIM offers significant benefits to project delivery standards, such as improvements in design quality [46], reduction in construction costs [47], and improvements in facility management [48]. Additionally, BIM provides an information enriched environment for predicting building performance, thus help improving sustainability throughout the building's lifecycle [49].

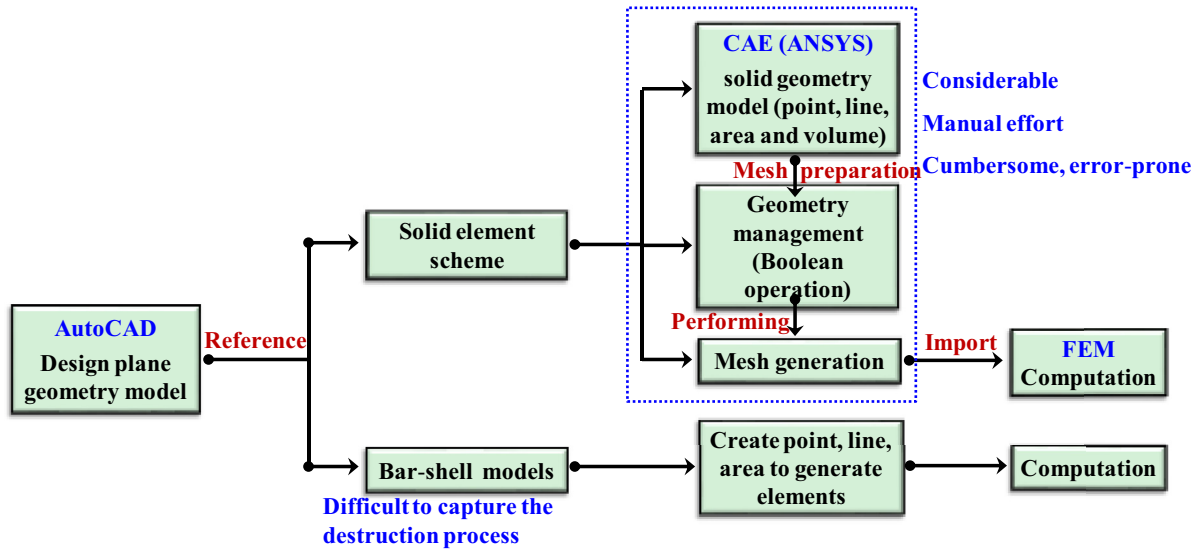


Fig. 2-1. Two design model for structural analysis.

In recognition of the benefits, BIM has recently been used to facilitate AEC education [50].

Currently, the most widely used commercial software in the field of architectural design is Revit [51]. Through a specialized structure analysis module (Revit Structure) [52], users can perform structural response analysis (e.g. Fig. 2-2). Despite the efficiency offered in analysis of the wire-frame model, the module method is not capable of capturing the process of failure. The conventional finite element solid analysis can solve the problem of presenting the structural failure, but it is very difficult to directly dissect the BIM solid model using the discrete element method, especially when hexahedrons are used. Therefore, it is difficult to integrate traditional FEM with the new and efficient BIM.

### 2.3. BIM-to-octree-to-SBFEM (highly efficient, automated, refined mesh, robust)

In order to begin process of integrating BIM with FEM, this section proposes a top-down design mode (namely BIM-to-Octree-to-SBFEM) to realize the efficient generation of spatial, structural model. A generic building structure is investigated as a representative example (explanatory flowchart is shown in Fig. 2-3).

In the top-down design mode, the model is derived directly from a BIM software (e.g. Revit, ArchiCAD, MicroStation) without spending much time on defining each point, line, plate, and volume. The BIM solid model can also directly be imported to the octree generator for performing efficient mesh discretization. However, another problem arises: due to the presence of polyhedron elements, traditional FEM cannot solve the grids generated from octree generator. Polyhedron formulations [53–57] are more versatile and flexible, and can overcome the element shape limitation of traditional FEM. Thus, polyhedrons are suitable candidates for solving the grids generated from octree generator. The advantages of both FEM and BEM thus synergized to create SBFEM, which provides a much more practical and flexible approach compared to its predecessors, especially when polyhedral elements are used. As will be seen in the following section, the SBFEM formulation is simple, easy to implement, and highly accurate.

## 3. Theory and element formulation

### 3.1. Formulation for polyhedron SBFEM

The detailed derivation of SBFEM has been introduced in the literature [8,58], and thus only the key equations are considered here. A

polygonal, mean-valued shape function  $\lambda$  formulated with local coordinates  $(\xi_1, \xi_2)$  is introduced to interpolate the boundary surface element. Then, a point  $(x, y, z)$  on the boundary face can be represented as

$$\begin{aligned} x(\xi_1, \xi_2) &= \lambda(\xi_1, \xi_2)\mathbf{x} \\ y(\xi_1, \xi_2) &= \lambda(\xi_1, \xi_2)\mathbf{y} \\ z(\xi_1, \xi_2) &= \lambda(\xi_1, \xi_2)\mathbf{z} \end{aligned} \quad (3.1)$$

where  $\mathbf{x}, \mathbf{y}, \mathbf{z}$  are the coordinate vectors located on the boundary. The scaling center  $\mathbf{O}(\hat{x}_0, \hat{y}_0, \hat{z}_0)$  and the boundary are connected using the defined radial coordinates  $\xi$ . In this manner, a point  $(\hat{x}, \hat{y}, \hat{z})$  inside the polyhedron can be described via SBFEM coordinates  $(\xi, \xi_1, \xi_2)$ :

$$\begin{aligned} \hat{x}(\xi, \xi_1, \xi_2) &= \xi\lambda(\xi_1, \xi_2)(x - \hat{x}_0) + \hat{x}_0 \\ \hat{y}(\xi, \xi_1, \xi_2) &= \xi\lambda(\xi_1, \xi_2)(y - \hat{y}_0) + \hat{y}_0 \\ \hat{z}(\xi, \xi_1, \xi_2) &= \xi\lambda(\xi_1, \xi_2)(z - \hat{z}_0) + \hat{z}_0 \end{aligned} \quad (3.2)$$

A transformation matrix  $\mathbf{J}_m$  is needed to map between SBFEM and local cartesian coordinates, which is given in equations below:

$$\mathbf{J}_m(\xi_1, \xi_2) = \begin{bmatrix} x(\xi_1, \xi_2) & y(\xi_1, \xi_2) & z(\xi_1, \xi_2) \\ x(\xi_1, \xi_2)_{,\xi_1} & y(\xi_1, \xi_2)_{,\xi_1} & z(\xi_1, \xi_2)_{,\xi_1} \\ x(\xi_1, \xi_2)_{,\xi_2} & y(\xi_1, \xi_2)_{,\xi_2} & z(\xi_1, \xi_2)_{,\xi_2} \end{bmatrix} \quad (3.3a)$$

$$|\mathbf{J}_m(\xi_1, \xi_2)| = x(y_{,\xi_1}z_{,\xi_2} - z_{,\xi_1}y_{,\xi_2}) + y(z_{,\xi_1}x_{,\xi_2} - x_{,\xi_1}z_{,\xi_2}) + z(x_{,\xi_1}y_{,\xi_2} - y_{,\xi_1}x_{,\xi_2}) \quad (3.3b)$$

where the derivatives are obtained from Eq. (3.1) as:

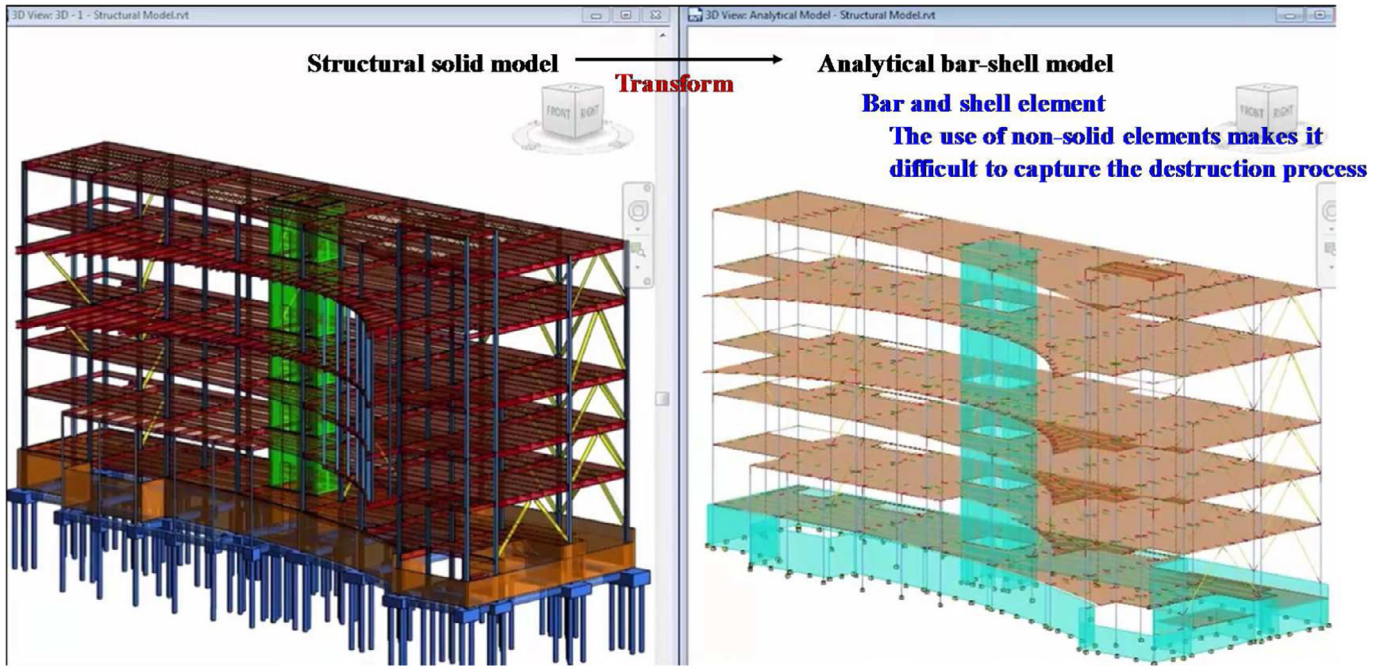
$$\begin{aligned} x(\xi_1, \xi_2)_{,\xi_1} &= \lambda(\xi_1, \xi_2)_{,\xi_1}\mathbf{x} \\ y(\xi_1, \xi_2)_{,\xi_1} &= \lambda(\xi_1, \xi_2)_{,\xi_1}\mathbf{y} \\ z(\xi_1, \xi_2)_{,\xi_1} &= \lambda(\xi_1, \xi_2)_{,\xi_1}\mathbf{z} \end{aligned} \quad (3.4a)$$

$$\begin{aligned} x(\xi_1, \xi_2)_{,\xi_2} &= \lambda(\xi_1, \xi_2)_{,\xi_2}\mathbf{x} \\ y(\xi_1, \xi_2)_{,\xi_2} &= \lambda(\xi_1, \xi_2)_{,\xi_2}\mathbf{y} \\ z(\xi_1, \xi_2)_{,\xi_2} &= \lambda(\xi_1, \xi_2)_{,\xi_2}\mathbf{z} \end{aligned} \quad (3.4b)$$

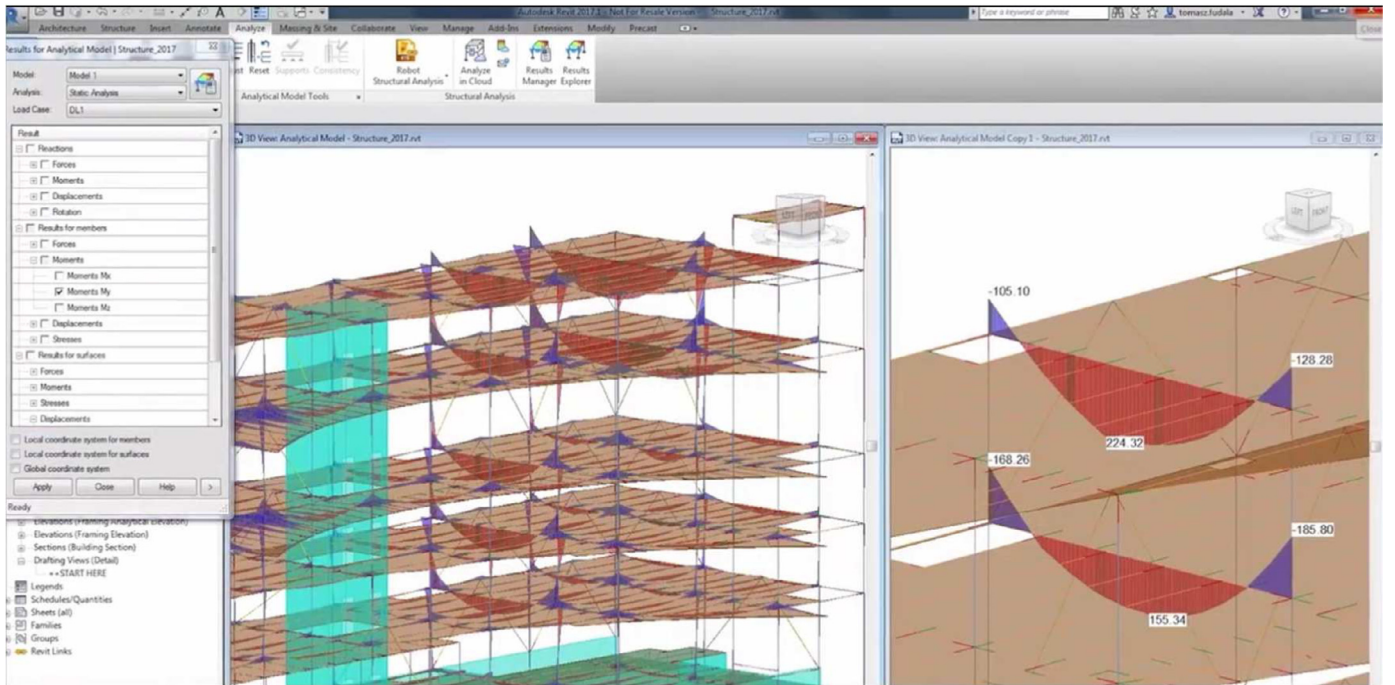
The gradient of the interpolation function with respect to the local coordinates is defined as  $\mathbf{LDu}$  and is defined in equation below

$$\mathbf{LDu} = \begin{bmatrix} \lambda(\xi_1, \xi_2) \\ \lambda(\xi_1, \xi_2)_{,\xi_1} \\ \lambda(\xi_1, \xi_2)_{,\xi_2} \end{bmatrix} \quad (3.5)$$





(a) Generate an analytical model (bar and shell element)



(b) Analyze and extract the results

Fig. 2-2. The analysis of a building in Revit structure.

The displacement components inside a pyramid can be described via a radial function  $u(\xi)$ , which is defined below

$$u(\xi, \xi_1, \xi_2) = \lambda^u(\xi_1, \xi_2)u(\xi) \quad (3.6a)$$

$$\lambda^u(\xi_1, \xi_2) = [\lambda_1[I], \lambda_2[I], \lambda_3[I], \lambda_4[I] \dots] \quad (3.6b)$$

where  $[I]$  is the  $3 \times 3$  identity matrix, and  $\lambda_i$  ( $i=1,2,3,\dots,n$ ) are the nodal displacement functions obtained by the canonical isoparametric technique. An equilibrium equation is extracted using the

mechanical equilibrium condition, where the unknown is the radial analytic function  $u(\xi)$

$$E_0 \xi^2 u(\xi)_{,\xi\xi} + (2E_0 + E_1^T - E_1) \xi u(\xi)_{,\xi} + (E_1^T - E_2) u(\xi) + F(\xi) = 0 \quad (3.7)$$

where the matrices  $E_0$ ,  $E_1$ , and  $E_2$  are temporary variables that depend only on the geometry and material properties.  $E_0$ ,  $E_1$ , and  $E_2$  are computed as follows:

$$E_0 = \int_{-1}^{+1} \int_{-1}^{+1} B_1^T D B_1 |J_m| d\xi_1 d\xi_2 \quad (3.8a)$$

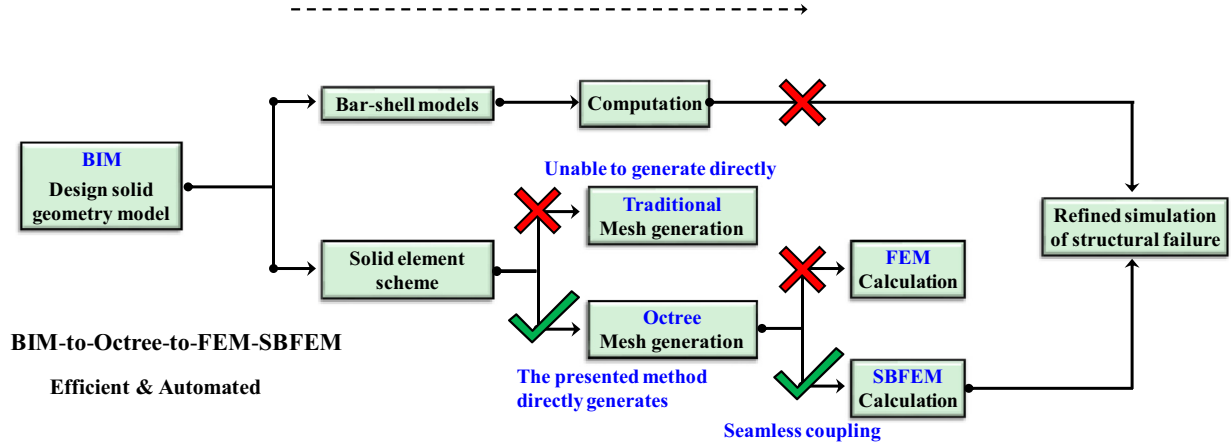


Fig. 2-3. Frame diagram of BIM structural design analysis.

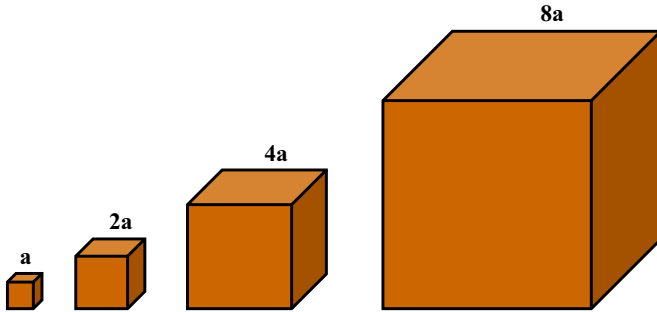


Fig. 3-1. The ratios of octree element size.

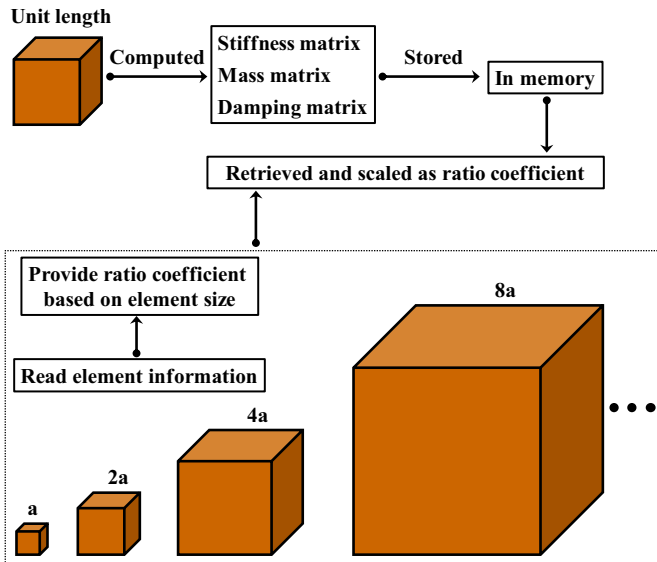


Fig. 3-2. Simple process of pre-computation.

$$\mathbf{M}_0 = \int_{-1}^{+1} \int_{-1}^{+1} \rho \lambda^T \lambda |\mathbf{J}_m| d\xi_1 d\xi_2 \quad (3.8d)$$

where  $\mathbf{B}_1$ ,  $\mathbf{B}_2$  and  $\mathbf{D}$  represents transition matrices and the material constitutive matrix, respectively.

Finally, the solution for the equilibrium equation is given in equation below

$$\mathbf{u}(\xi) = \boldsymbol{\psi}_u \xi^{-(0.5+S_n)} \mathbf{c} \quad (3.9)$$

where  $S_n$  is a diagonal matrix, and its entries are composed of the real parts of the eigenvalues. The matrix  $\boldsymbol{\psi}_u$  is composed of the modal displacements. The coefficient  $\mathbf{c}$  can be obtained from the boundary nodal displacement vector  $\mathbf{u}_b = \mathbf{u}(\xi = 1)$

$$\mathbf{c} = \boldsymbol{\psi}_u^{-1} \mathbf{u}_b. \quad (3.10)$$

Substituting Eq. (3.10) into Eq. (3.9),  $\mathbf{u}(\xi)$  can be solved by

$$\mathbf{u}(\xi) = \boldsymbol{\psi}_u \xi^{-S_n-0.5} \boldsymbol{\psi}_u^{-1} \mathbf{u}_b. \quad (3.11)$$

Substituting Eq. (3.11) into Eq. (3.6a), the displacement field  $\mathbf{u}(\xi, \xi_1, \xi_2)$  can be evaluated by

$$\mathbf{u}(\xi, \xi_1, \xi_2) = (\lambda^u(\xi_1, \xi_2) \boldsymbol{\psi}_u \xi^{-(0.5+S_n)} \boldsymbol{\psi}_u^{-1}) \mathbf{u}_b. \quad (3.12)$$

Finally, the polyhedral interpolation function  $\Phi(\xi, \xi_1, \xi_2)$  is expressed as

$$\Phi(\xi, \xi_1, \xi_2) = \lambda^u(\xi_1, \xi_2) \boldsymbol{\psi}_u \xi^{-(0.5+S_n)} \boldsymbol{\psi}_u^{-1}. \quad (3.13)$$

Using the strain formulation provided by Wolf and Song [11], the expression for the strain of a polyhedron can be obtained by substituting the formulation into Eq. (3.11)

$$\begin{aligned} \boldsymbol{\varepsilon}(\xi, \xi_1, \xi_2) &= (\mathbf{B}_1(\xi_1, \xi_2) \boldsymbol{\psi}_u (-S_n - 0.5) \xi^{-(1.5+S_n)} \boldsymbol{\psi}_u^{-1}) \mathbf{u}_b \\ &\quad + \left( \frac{1}{\xi} \mathbf{B}_2(\xi_1, \xi_2) \boldsymbol{\psi}_u \xi^{-(0.5+S_n)} \boldsymbol{\psi}_u^{-1} \right) \mathbf{u}_b. \end{aligned} \quad (3.14)$$

Extracting the coefficient before  $\mathbf{u}_b$ , the strain computed by SBFEM can be simplified as

$$\boldsymbol{\varepsilon}(\xi, \xi_1, \xi_2) = \mathbf{B}(\xi, \xi_1, \xi_2) \mathbf{u}_b \quad (3.15a)$$

$$\begin{aligned} \mathbf{B}(\xi, \xi_1, \xi_2) &= (\mathbf{B}_1(\xi_1, \xi_2) \boldsymbol{\psi}_u (-S_n - 0.5) \xi^{-(1.5+S_n)} \boldsymbol{\psi}_u^{-1}) \\ &\quad + \left( \frac{1}{\xi} \mathbf{B}_2(\xi_1, \xi_2) \boldsymbol{\psi}_u \xi^{-(0.5+S_n)} \boldsymbol{\psi}_u^{-1} \right) \end{aligned} \quad (3.15b)$$

where  $\mathbf{B}(\xi, \xi_1, \xi_2)$  is the strain-displacement matrix of a polyhedron.

$$\mathbf{E}_1 = \int_{-1}^{+1} \int_{-1}^{+1} \mathbf{B}_2^T \mathbf{D} \mathbf{B}_1 |\mathbf{J}_m| d\xi_1 d\xi_2 \quad (3.8b)$$

$$\mathbf{E}_2 = \int_{-1}^{+1} \int_{-1}^{+1} \mathbf{B}_2^T \mathbf{D} \mathbf{B}_2 |\mathbf{J}_m| d\xi_1 d\xi_2 \quad (3.8c)$$

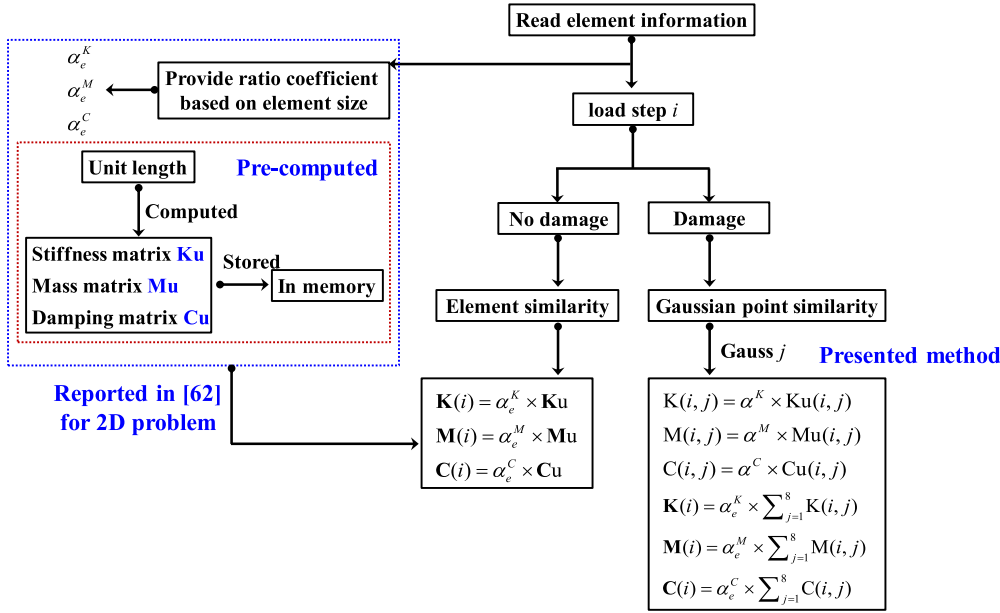


Fig. 3-3. Flowchart for solving problems using nonlinear, similar elements [62].

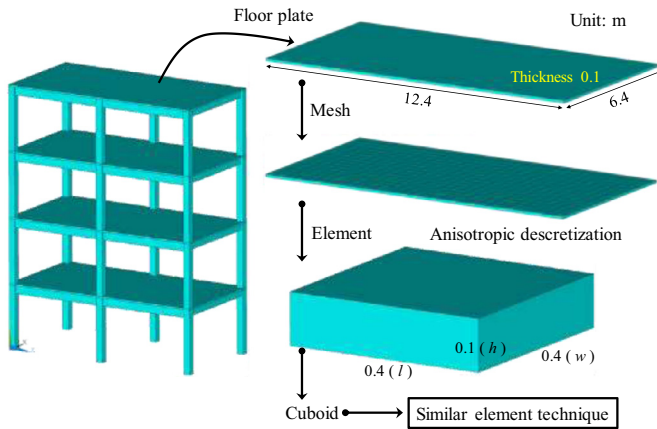


Fig. 3-4. Discrete illustration of anisotropic meshes.

In elasto-plastic analysis, the incremental strain field can be decomposed into incremental elastic and plastic strain components. The plastic strain increment can then be determined from the plastic flow rule. Assuming associative plasticity and using the yield functions  $F$  and plastic

multiplier  $\Delta\lambda$ , the plastic strain increment can be expressed as

$$\begin{aligned} \Delta\epsilon &= \Delta\epsilon_e + \Delta\epsilon_p \\ \Delta\epsilon_p &= \frac{\partial F}{\partial \sigma} \Delta\lambda \end{aligned} \quad (3.16)$$

where  $F = F(\sigma, \kappa)$  is defined as the yield function and is determined from the current stress state  $\sigma$  and the hardening parameter  $\kappa$ . Using Hooke's law, the incremental stress field  $\Delta\sigma$  can be written as

$$\Delta\sigma = \mathbf{D}_{ep} \Delta\epsilon \quad (3.17)$$

where  $\mathbf{D}_{ep}$  is the elasto-plastic constitutive matrix. Substituting Eq. (3.15a) into the formulation for the incremental strain field  $\Delta\epsilon$  (Eq. (3.16)), the incremental stress field is expressed as

$$\Delta\sigma(\xi, \xi_1, \xi_2) = \mathbf{D}_{ep} \mathbf{B}(\xi, \xi_1, \xi_2) \Delta\mathbf{u}_b \quad (3.18)$$

where  $\Delta\mathbf{u}_b$  is the incremental nodal displacement on the boundary.

Subsequently, the equation for the elastic-plastic strain of scaled boundary polyhedron elements can be derived from the principle of virtual work, as shown in equation below,

$$\int_{\Omega} \delta \epsilon^T \Delta\sigma(\xi, \xi_1, \xi_2) d\Omega = \int_{\Gamma} \delta \mathbf{u}^T \mathbf{f}_t d\Gamma + \int_{\Gamma} \delta \mathbf{u}^T \mathbf{f}_b d\Gamma - \int_{\Omega} \delta \epsilon^T \sigma(\xi, \xi_1, \xi_2) d\Omega \quad (3.19)$$

where  $\Delta\sigma(\xi, \xi_1, \xi_2)$  is the incremental stress (Eq. (3.18)),  $\mathbf{f}_t$  and  $\mathbf{f}_b$  represent the surface traction and intensity of body forces, respectively,

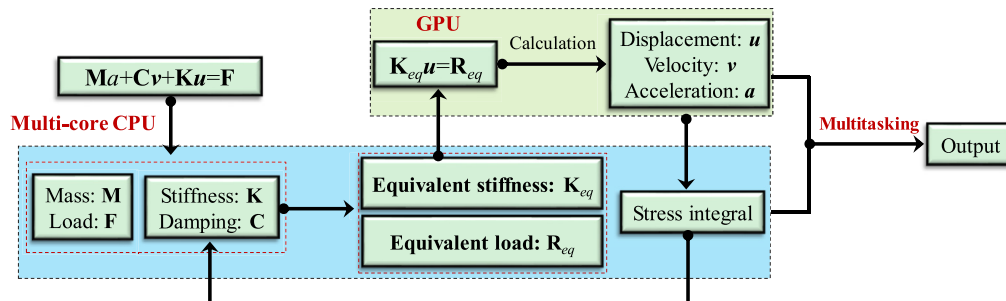


Fig. 3-5. Heterogeneous parallel computing framework using both CPU and GPU.

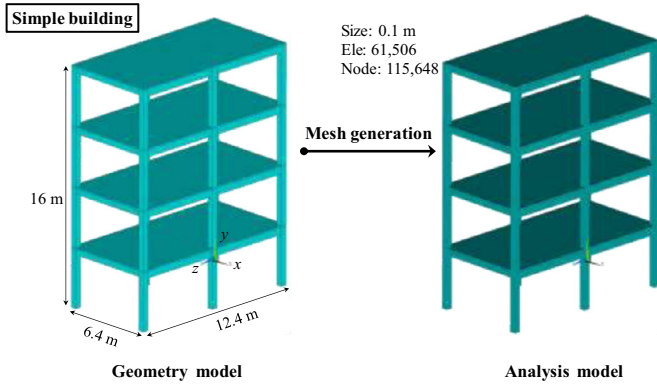


Fig. 4-1. The geometry and analysis model.

and  $\delta\epsilon(\xi, \xi_1, \xi_2)$  is the virtual strain field corresponding to the virtual displacement field  $\delta u(\xi, \xi_1, \xi_2)$ . By substituting the equations for these variables, the detailed formula of Eq. (3.19) can be rewritten as shown in equation below.

$$\begin{aligned} & \left( \int_{\Omega} \mathbf{B}^T(\xi, \xi_1, \xi_2) \mathbf{D}_{ep} \mathbf{B}(\xi, \xi_1, \xi_2) d\Omega \right) \Delta \mathbf{u}_b \\ &= \left( \int_{\Gamma} \Phi^T(\xi, \xi_1, \xi_2) \mathbf{f}_i d\Gamma + \int_{\Gamma} \Phi^T(\xi, \xi_1, \xi_2) \mathbf{f}_b d\Omega \right) \\ & \quad - \left( \int_{\Omega} \mathbf{B}^T(\xi, \xi_1, \xi_2) \boldsymbol{\sigma}(\xi, \xi_1, \xi_2) d\Omega \right) \end{aligned} \quad (3.20)$$

The first set of parentheses on the left-hand side of Eq. (3.20) is the elasto-plastic stiffness matrix  $\mathbf{K}_{ep}$ , the second term is the external load vector  $\mathbf{R}_{ext}$ , and the last term is the internal load vector  $\mathbf{R}_{int}$ . Thus, Eq. (3.20) can be simplified as

$$\mathbf{K}_{ep} \Delta \mathbf{u}_b = \mathbf{R}_{ext} - \mathbf{R}_{int} \quad (3.21)$$

Eq. (3.21) is a system of nonlinear equilibrium equations which can be assembled element-by-element. The equilibrium equation of the

Table 3-1

Comparison of computational effort between the similar element method and conventional method.

Computation method	Status	Multiplication	Addition
Similar element: $\mathbf{K} = \alpha_e^K \times [\mathbf{K}_u]_{24 \times 24}$	Elastic	577	0
$\mathbf{K} = \alpha_e^K \sum_{i=1}^8 \alpha_i^K \times \mathbf{K} u_i$	Damaged	4624	4608
Conventional method: $\mathbf{K} = \sum_{i=1}^8 [\mathbf{B}_i^T]_{24 \times 6} [\mathbf{D}]_{6 \times 6} [\mathbf{B}_i]_{6 \times 24} dV_i$		34,560	39,168

problem domain is defined as

$$\left( \sum_{i=1}^{nPol} \mathbf{K}_{ep} \right) \Delta \mathbf{U}_b = \sum_{i=1}^{nPol} (\mathbf{R}_{ext} - \mathbf{R}_{int}) \quad (3.22)$$

where  $\Delta \mathbf{U}_b$  is the incremental nodal displacement vector on the boundary of the entire domain, and  $nPol$  represents number of integration points in all polyhedrons. Standard nonlinear iterative solvers, such as the modified Newton–Raphson method, can be employed to solve this Eq. (3.22).

### 3.2. Plastic-damage model for concrete material

In this paper, the concrete of a frame structure is modeled using the Lee–Fenves model, which can describe the damage propagation process. The main components of the model are discussed here. Interested readers can find a more detailed derivation in [59,60].

The total strain  $\epsilon$  is decomposed into two parts in the theory of plasticity:

$$\epsilon = \epsilon^e + \epsilon^p \quad (3.23)$$

where  $\epsilon^e$  and  $\epsilon^p$  represent the elastic and the plastic components, respectively. Then, the stress–strain relationship is defined as

$$\boldsymbol{\sigma} = (1 - D) \bar{\boldsymbol{\sigma}} = (1 - D) E_0 : (\epsilon - \epsilon^p) \quad (3.24)$$

where  $\bar{\boldsymbol{\sigma}}$  is the effective stress,  $E_0$  is the undamaged elastic stiffness, and  $D$  is a scalar parameter that reflects decreased elastic stiffness (i.e. damage degradation).

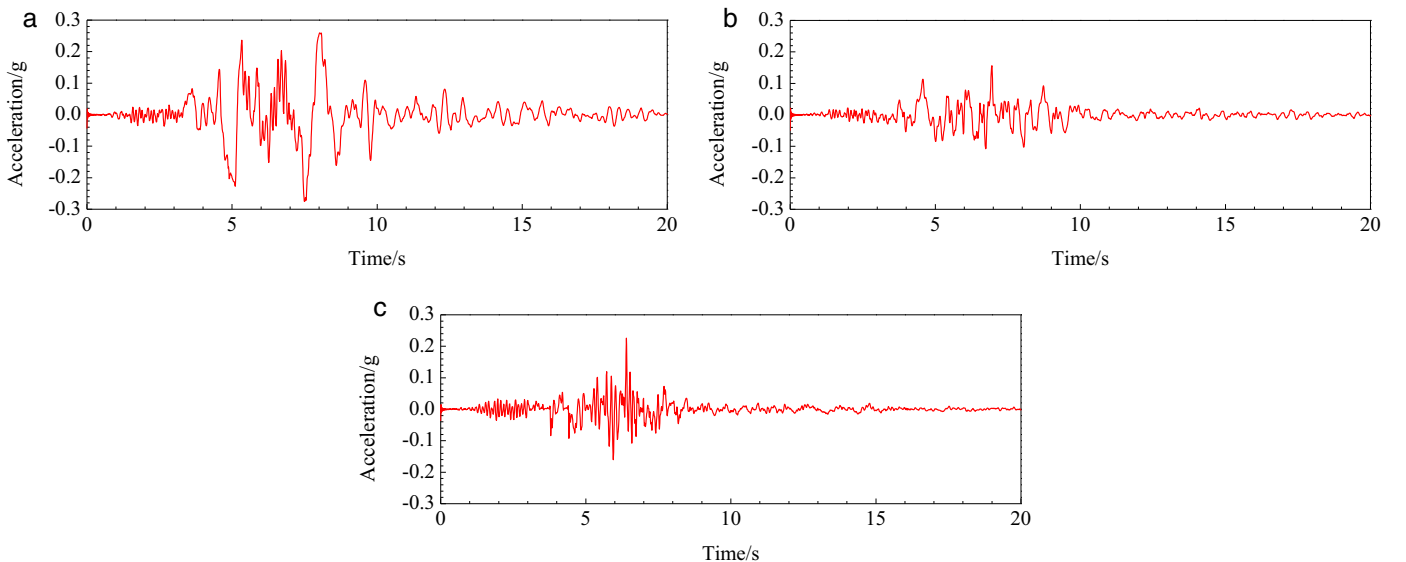


Fig. 4-2. Input excitation: (a) x-direction, (b) y-direction and (c) z-direction.



The total strength, which is determined by the plastic strain in Lubliner et al. [61], and the corresponding formula is expressed as

$$\sigma_{\mathfrak{N}}(\epsilon^p) = f_{\mathfrak{N}0}[(1 + a_{\mathfrak{N}})\exp(-b_{\mathfrak{N}}\epsilon^p) - a_{\mathfrak{N}}\exp(-2b_{\mathfrak{N}}\epsilon^p)] \quad (3.25)$$

where  $f_{\mathfrak{N}0}$  is the initial yield strength, and  $a_{\mathfrak{N}}$ ,  $b_{\mathfrak{N}}$  are constants.  $\mathfrak{N} = t$  indicates uniaxial tension state, while the state of uniaxial compression is represented by  $\mathfrak{N} = c$ .

The parameter  $\kappa_{\mathfrak{N}}$  expresses the state of damage, and is defined as follows:

$$\kappa_{\mathfrak{N}} = \frac{1}{g_{\mathfrak{N}}} \int_0^{\epsilon^p} \sigma_{\mathfrak{N}}(\epsilon^p) d\epsilon^p; \quad g_{\mathfrak{N}} = \int_0^{\infty} \sigma_{\mathfrak{N}}(\epsilon^p) d\epsilon^p \quad (3.26)$$

where  $g_{\mathfrak{N}}$  represents the density of dissipated energy as micro-cracks nucleate and propagate.  $g_{\mathfrak{N}}$  can also be derived from the ratio of the fracture energy  $G_{\mathfrak{N}}$  [61] to the characteristic length  $l_{\mathfrak{N}}$  (i.e.,  $g_{\mathfrak{N}} = G_{\mathfrak{N}}/l_{\mathfrak{N}}$ ) [61].

Additionally, to describe the opening and closing behaviour of the crack, a weight factor  $s$  is introduced. Then the degradation damage parameter  $D$  in Eq. (3.24) can be rewritten as

$$D = 1 - (1 - D_c(\kappa_c))(1 - sD_t(\kappa_t)) \quad (3.27)$$

### 3.3. Element similarity technique

As reported in [8,58], the grids consist of cubes and polyhedrons. One of the primary advantages of using octree discretization is that cubical elements occupy a major proportion of the elements in the mesh. Throughout the grids, a 2:1 mesh ratio is implemented (i.e. size ratio between two adjacent cells is 2). The dimensions of the elements are proportional, as shown in Fig. 3-1.

In order to improve the computational efficiency by taking advantage of the similarity among the grids, we propose the 3D element similarity technique. At the current stage, only the similarity of cube elements will be considered. In theory other types elements with hanging nodes can also be similar to each other, but their discussion is beyond the scope of this paper.

As shown in Fig. 3-2, for applications in homogeneous isotropic materials, the matrix of one unit cube can be pre-computed and stored in the background memory. The matrix or matrices are subsequently retrieved as a ratio coefficient during each load step. The detailed process is shown in Fig. 3-3.

First, the ratio coefficients ( $\alpha_e^K$ ,  $\alpha_e^M$ ,  $\alpha_e^C$ ) of each element is obtained according to the element size. Then at each load step, the damage status is judged according to the damage factor. If no damage has occurred, the stiffness matrix, the mass matrix, and the damping matrix are obtained directly from the pre-computed parameters (stiffness, mass, and damping matrices) in memory according to the ratio coefficient. This strategy has been reported in [61] for elastic problems. If the element is damaged, the parameters of each Gaussian point are computed according to the coefficients of modulus degradation ( $\alpha^K(i, j)$ ,  $\alpha^M(i, j)$ ,  $\alpha^C(i, j)$ , where  $i$  is the load step and  $j$  represents the Gaussian point). Then the summation of all Gaussian points can be carried out, and the parameters can be obtained after the damage has occurred. The method developed in this paper can perform such similarity-based computations for elastic conditions (at the element level). For nonlinear damage, the similarity of Gaussian points can also be used. In general, this method reduces the computation time of Lee–Fenves plastic damage and optimizes the efficiency of seismic destruction analyses.

The similar element technique saves a large amount of computational resources. As shown in Table 3-1, when the element is in the elastic state, only 577 multiplications are needed to obtain the element stiffness matrix. Only 4624 multiplications and 4608 addition operations are required to solve and obtain the damaged status. However, by using the conventional method, 34,560 multiplications and 39,168 additions are necessary to obtain the elemental stiffness matrix. The computational resources required for conventional methods thus far outweigh the requirements when the similarity technique is used instead.

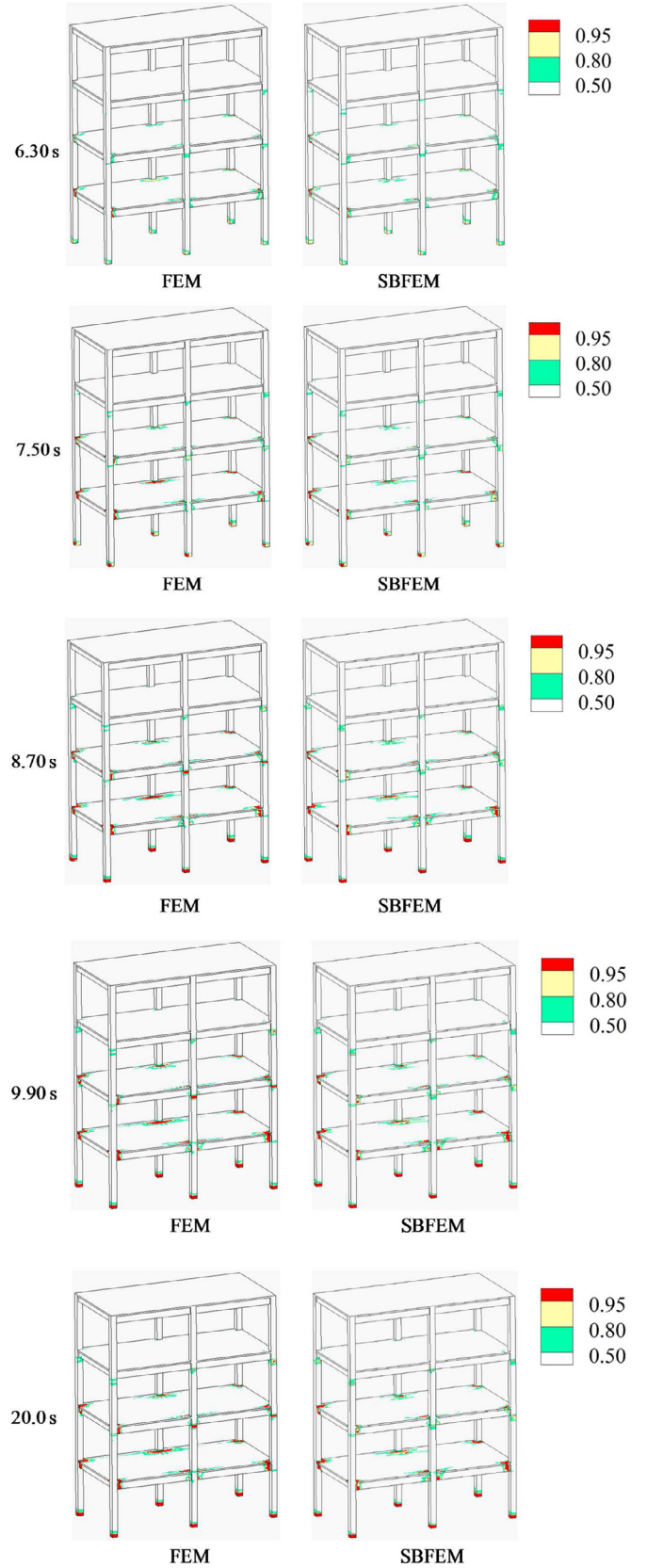


Fig. 4-3. Distribution of tensile damage of representative time using FEM and SBFEM.



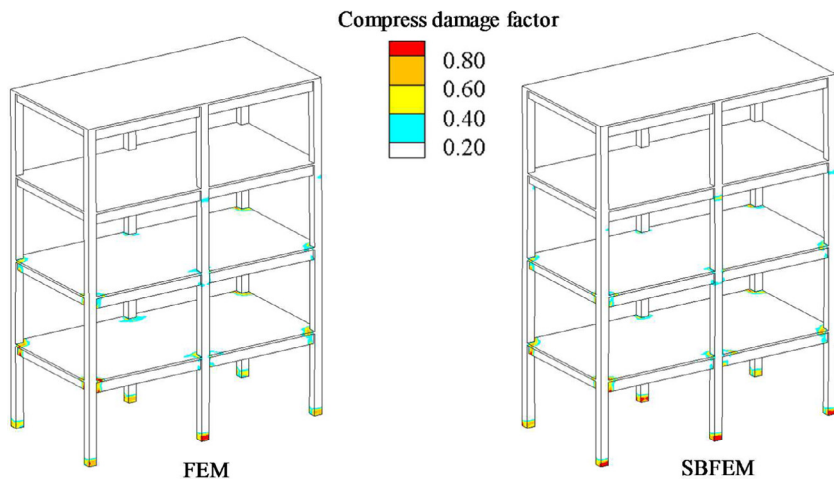


Fig. 4-4. Distribution of compression damage after earthquake.

Additionally, the building floors are treated differently since the dimension along thickness direction ( $h$ ) is quite different from the other directions, as shown in Fig. 3-4. The maximum difference can be as large as 124 times. For such structures, it is a more computationally economical alternative to use anisotropic discretization (discrete, nonuniform dimensions for each direction). If rectangular parallelepiped elements are used, the number of elements can be reduced, thus leading to a decrease in the computation time. Moreover, the cuboid elements can also use element similarity to improve the efficiency of the solution step. As long as the length  $l$ , width  $w$  and height  $h$  meet a uniform ratio, the element stiffness matrix can be obtained by using the similarity coefficient for saving computational costs. This paper mainly discusses the application of the similarity technique for cube elements.

### 3.4. CPU+GPU parallel computation

The graphic processing unit (GPU) is extremely efficient in solving large systems of equations. Therefore, a high-performance GPU graphics card (NVIDIA Tesla V100) is used to accelerate the solution process. Fig. 3-5 illustrates how parallel CPU and GPU computation can be used to speed up the solution process. Further, through using the multitasking output mode to avoid delays associated with writing information to the disk, the augmented solver is nearly 8 times faster than with using traditional CPU multi core parallel solver.

## 4. Verification and application

### 4.1. Verification of simple frame building

#### 4.1.1. Model and parameters

A four-storey concrete frame structure with the height of 16 m was selected for analysis and for verifying the methods described in Section 3. The geometry is shown in Fig. 4-1. The structure is 6.4 m and 16 m long in the  $x$  and  $y$  directions, respectively. The length in the  $z$ -direction is 12.4 m across two spans. The height of each floor is 3.9 m, the thickness of the plate is 0.1 m, the beam section size is  $0.2 \text{ m} \times 0.4 \text{ m}$ , and the column section is  $0.4 \text{ m} \times 0.4 \text{ m}$ . A refined grid scheme where each element is 0.1 m in length, thus leading to 61,506 elements, and 346,944 DOFs.

A 3D FEM and SBFEM analysis program, GEODYNA, developed by Zou et al. [63] and used in many prior studies [64–68], is employed in this paper. The isoparametric element, scaled boundary polyhedron FEM, plastic damage constitutive models and the solution methods mentioned in Section 3 have been incorporated into GEODYNA. In this section, in order to verify the program, traditional isoparametric FEM and SBFEM were used to separately conduct the seismic damage analysis.

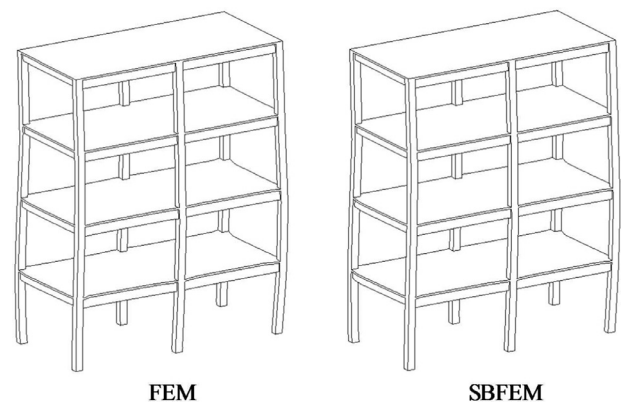


Fig. 4-5. Deformation pattern of two methods (Magnified 10 times).

The concrete material was described using the plastic damage model [59,60], and the parameters were defined as follows: density  $\rho = 2400 \text{ kg/m}^3$ , elastic modulus  $E = 30.0 \text{ GPa}$ , Poisson's ratio  $\nu = 0.18$ , ultimate compressive strength  $f_c = 25.6 \text{ MPa}$ , and ultimate tensile strength  $f_t = 2.0 \text{ MPa}$ .

#### 4.1.2. Input ground motion

A Hanshin earthquake record with maximum accelerations of 0.276 g, 0.156 g and 0.226 g along the  $x$ -,  $y$ - and  $z$ -directions, respectively, was used as the excitation with time steps of 0.01 s. The acceleration records of the seismic waves are shown in Fig. 4-2.

#### 4.1.3. Results

The distribution of primary tensile damage using FEM and SBFEM are shown in Fig. 4-3. As can be seen in the figure, when the structure has been excited for 6.3 s, tensile damage can be observed in the corners within the structure. Then, at 7.5 s and 8.7 s, the damage distribution increased gradually and concentrated at the intersections of beams, columns and plates. From 9.9 s to the end of the analysis, the distribution range of damage remained essentially the same. The main reason that not much change was observed anymore is that the peak intensity of the earthquake is mainly concentrated between 5 s and 10 s. Thus the bulk of the tensile damage inflicted upon the structure occurred during this time. Beyond 10 s, the excitation intensity rapidly reduced and consequently, the vibration of the structure was also reduced, thus limiting the progression and distribution of damage.

The distribution of compressive damage and the structural deformations are shown in Figs. 4-4 and 4-5. As can be observed from the figures, there is a significant compressive damage at the bottom corners and the

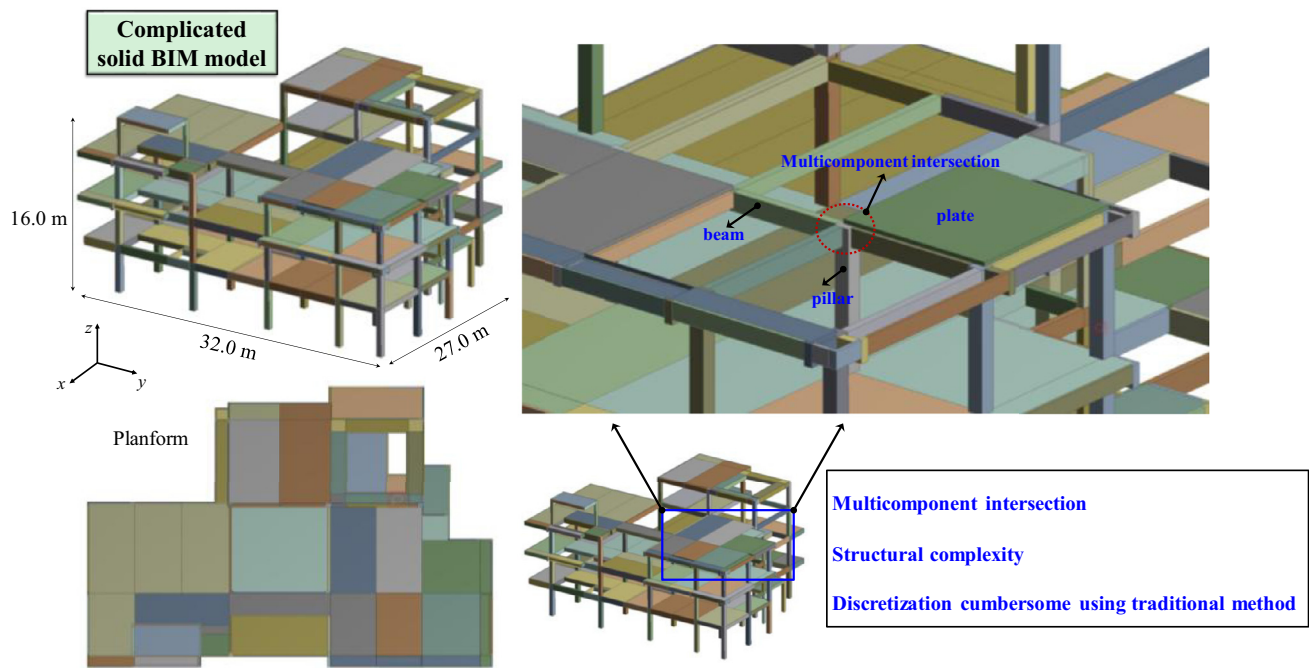


Fig. 4-6. Geometry of a complicated frame structure.

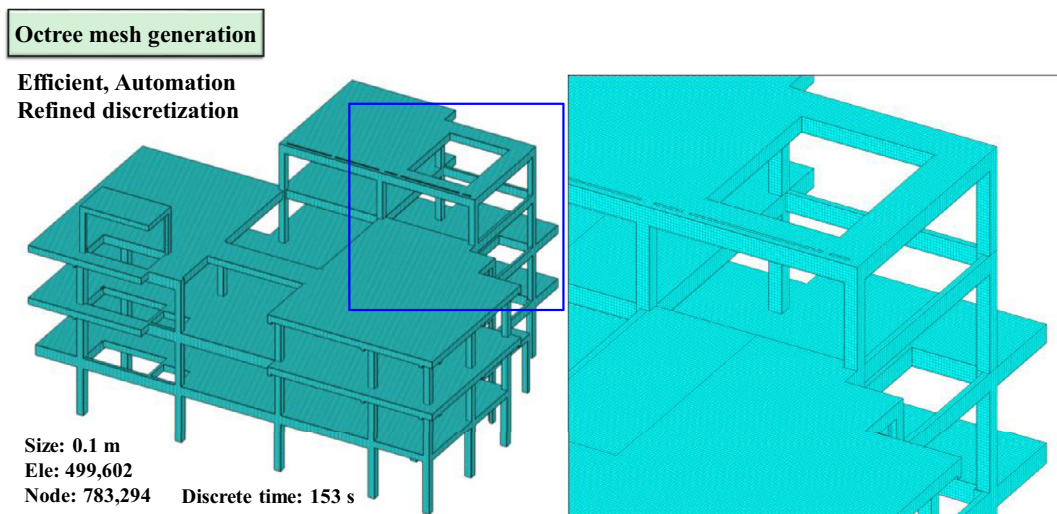


Fig. 4-7. Mesh discretization using Octree algorithm (element size 0.1 m).

end of the columns because the bottom storey was subjected to the maximum load. The distribution of damage computed by the two methods are consistent, and only the exact values of the local damage is different (e.g. SBFEM returned slightly larger values than FEM).

The deformation patterns are also consistent between the two methods. Fig. 4-5 shows that the SBFEM can be as convenient as the traditional isoparametric FEM for simulating structural seismic responses. The consistency between the results verify the accuracy and feasibility of SBFEM.

## 4.2. Application of a complex BIM model

### 4.2.1. Geometry and efficient discretization

In order to demonstrate the advantages of the proposed method in modeling complex models, a detailed seismic analysis of frame structure generated from BIM was carried out. Fig. 4-6 shows the model geometry and the corresponding dimensions. The model is 32 m along the

y-direction, 27 m in the x-direction and 16 m in the z-direction. There are many components in the model, and the beams, columns and plates intersect frequently to form a complex structure, thus leading to a more cumbersome and time-consuming discretization process.

This paper uses an efficient octree generator to discretize the complex model. The primary advantage of the generator is that the BIM entity model can be directly imported to generate grid information. Figs. 4-7–4-9 show three different grid sizes used during discretization. The results show that the automated octree discretization technique is highly efficient, with only a few minutes required for the different discretizations. The technique was rapid especially for secondary modifications (e.g. different discretization sizes, local refinement) of the computational model. A grid density of 0.1 m was selected for the analysis model.

As shown in Fig. 4-7, the minimum size of the element is 0.1 m, resulting in 499,602 elements and 2349,882 DOFs; it is worth noting that the entire discretization process took only 153 s. Another notable feature



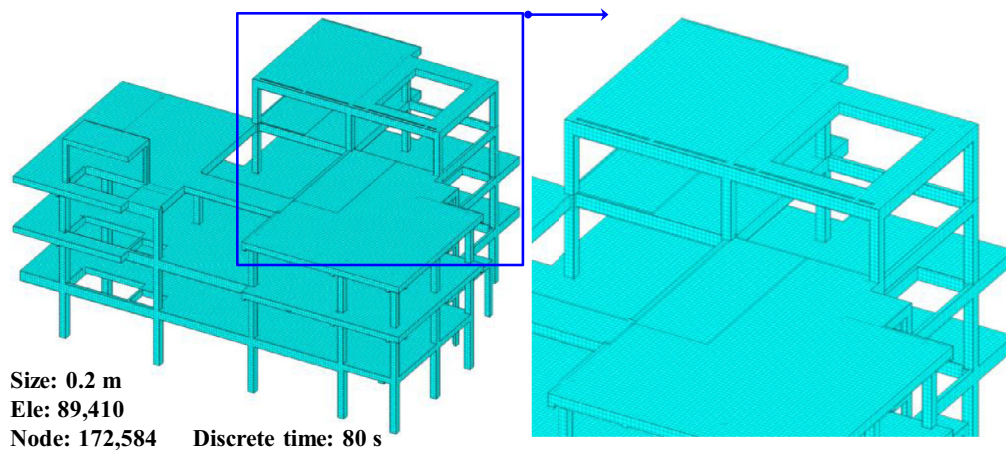


Fig. 4-8. Mesh discretization using Octree algorithm (element size 0.2 m).

is that since the frame structure is relatively regular, the hexahedrons comprised 95.31% of the model. Out of the hexahedrons, the proportion of cube elements was 82.2%. With the similar element method used to improve the solution efficiency, the number of polyhedrons was only 4.69% (see Table 1). In addition, the SBFEM-FEM coupling procedure was used, where the hexahedral elements are computed via FEM, and a small amount of polyhedron elements is solved by SBFEM. This division of labor ensures efficiency throughout the computational processes.

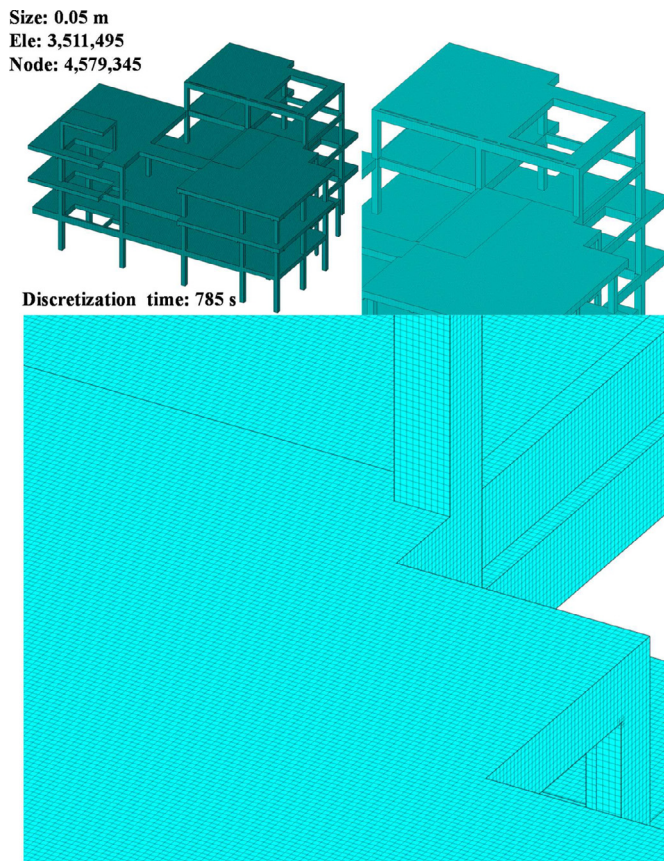


Fig. 4-9. Information of octree mesh discretization (element size 0.05 m).

#### 4.2.2. Parameters and results

The concrete material was represented by the plastic damage model [59,60], and the parameters were defined as follows: density  $\rho=2400 \text{ kg/m}^3$ , elastic modulus  $E=30.0 \text{ GPa}$ , Poisson's ratio  $\nu=0.18$ , ultimate compressive strength  $f_c=25.6 \text{ MPa}$ , and ultimate tensile strength  $f_t=2.0 \text{ MPa}$ . The time history curve of Fig. 4-2 was used as the input in the form of ground motion, and the time interval was set to 0.01 s.

Fig. 4-10 shows the overall distribution of tensile damage at selected times. As can be seen, structural failure occurred during peak acceleration. At 6.3 s, the structure exhibited obvious signs of damage, and then at 7.9 s and 8.7 s, the degree and scope of damage increased considerably. From 9.9 s onwards, the earthquake record, while active, was essentially subsided. Thus from 9.9 s to 20 s, the damage distribution did not change much. In general, the damage distribution was concentrated at the intersection between the bottom columns and the floor, as well as at the intersections among beams and columns. Such a distribution may be expected from the perspective of structural mechanics.

Fig. 4-11 show the damage distribution from another perspective and Fig. 4-12 shows the overall deformation along with the tensile and compressive damages. As suggested by the figures, there is serious damage to the end and left plate of the bottom column, the main reason being that the bottom load was large. The left end is an overhanging plate, and its structural similarity to a cantilever beam makes it prone to yielding. The oscillating action of the earthquake load easily induced a stress concentration at the end of the plate and thus inflicted damage. Therefore, corresponding reinforcement should be implemented in such areas to mitigate potential earthquake damage.

Fig. 4-13 shows the location of the destruction in a similar type of structure in the actual earthquake. The photos captured severe damage at the end of the columns and at the intersections of the multi-component junctions. The bottom structure was burdened with the greatest load and suffered the most damage, thus leading to an inevitable collapse. This phenomenon is highly consistent with the above numerical simulation, which indicates the accuracy and applicability of the proposed method.

Efficient and simple local refinement of the interested region is the primary advantage of the octree discretization. Based on the preliminary computation results, the local structure can be further refined in severely damaged areas (Fig. 4-14). The refinement in local structure can provide guidance for the optimization of the structural design. In addition, Table 2 lists the detailed grid type statistics. The ratio of conventional hexahedron elements is 95.31%, and the proportion of cube grids from among the hexahedron elements is approximately 85%, which demonstrates that the quality of the generated mesh is very high.

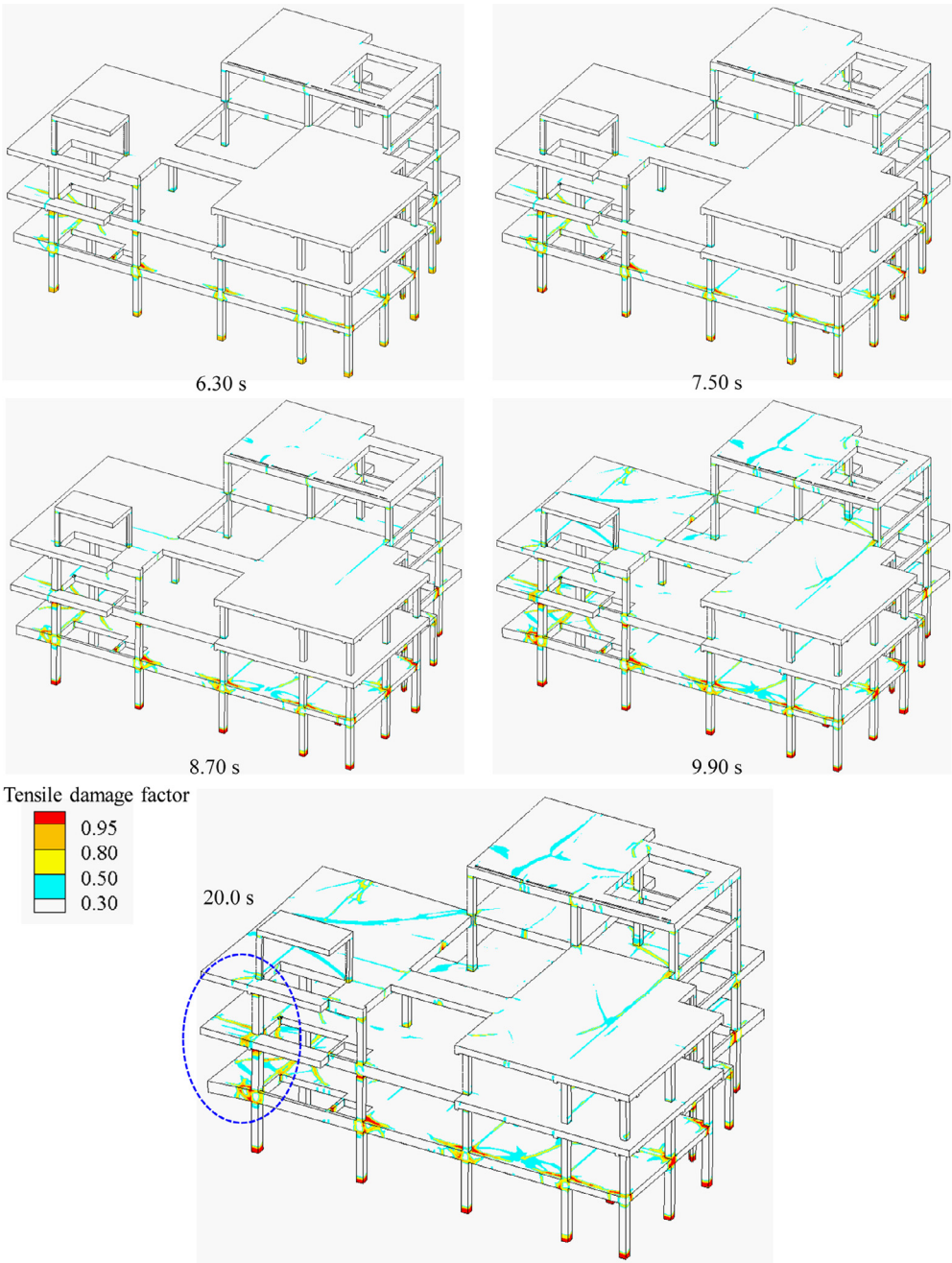


Fig. 4-10. Distribution of tensile damage of representative time using SBFEM.

**Table 1**  
Statistics of the element types in the frame building model with an octree discretization.

Element types	Faces in one element	Number	Percentage (%)	Sum (%)
Hexahedron	Cube	410,688	82.20	95.31
	Non-cube	65,473	13.11	
Polyhedron	>6	23,441	4.69	4.69

**Table 2**  
Statistics of the element types in the frame building model with another octree discretization.

Element types	Faces in one element	Number	Percentage (%)	Sum (%)
Hexahedron	Cube	479,483	84.37	95.31
	Non-cube	67,459	11.87	
Polyhedron	>6	21,368	3.76	3.76



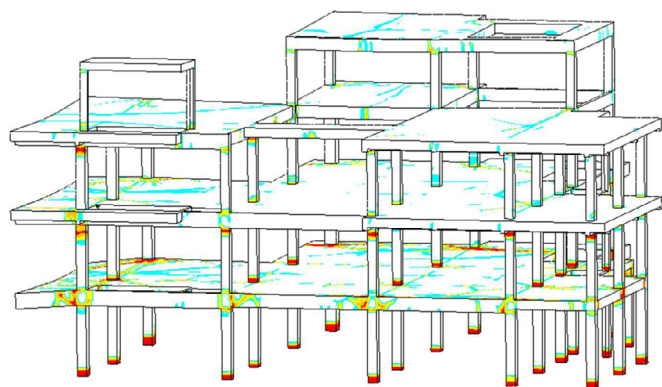


Fig. 4-11. Distribution of tensile damage from another perspective (20.0 s).

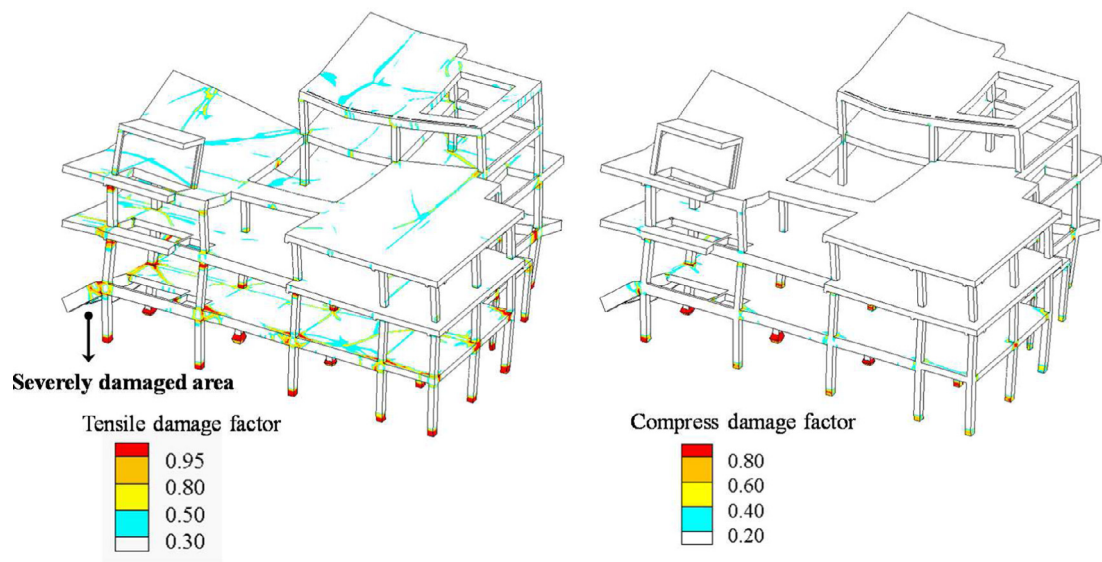


Fig. 4-12. Distribution of damage with deformation (Magnified by 10 times).



Frame damage at the bottom of a column



Frame damage at the top of a column



Damage of frame structure in beam



Collapse of the first floor in a frame structure

Fig. 4-13. Failure of a frame structure building similar to the one used during simulation.

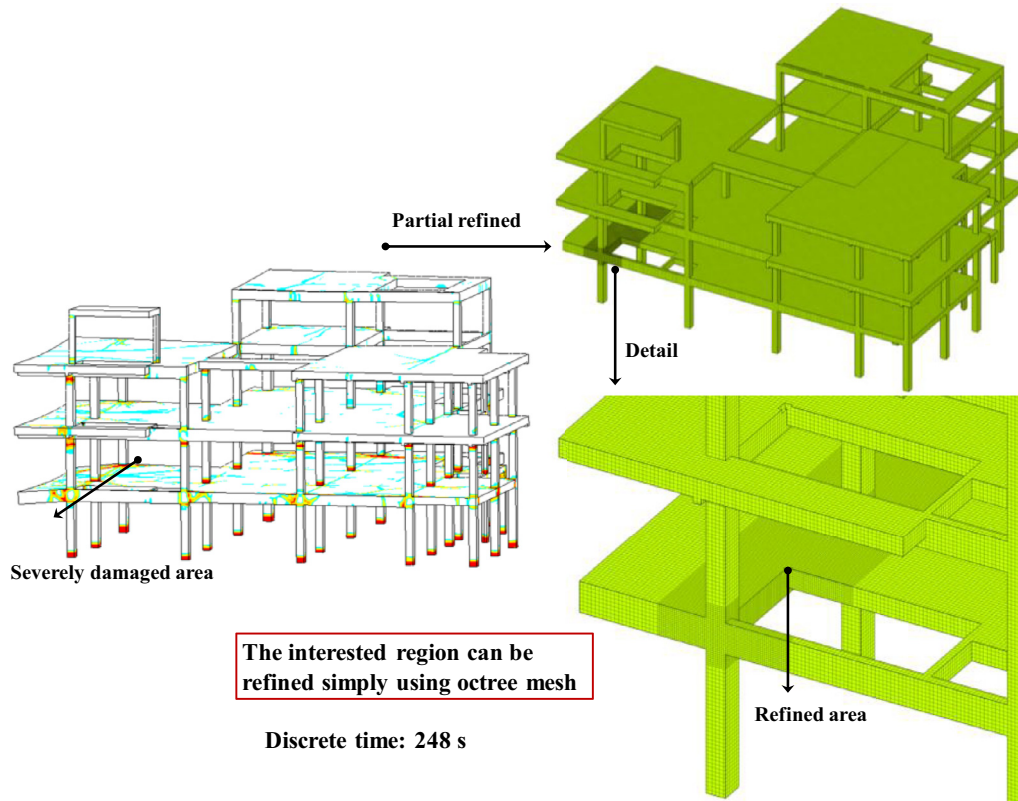


Fig. 4-14. Mesh refinement for the interested region.

## 5. Conclusion

The proposed BIM-to-Octree-to-FEM-SBFEM (BOFSM) methodology allows the highly efficient generation of complex geometry and analysis of structural response. First the geometry is generated and automatically using BIM. The geometry is subsequently converted into an octree discretization for rapid simulation of the structural damage process. In order to speed up the simulation, the following features were used: coupled and scaled boundary polyhedron finite element analysis, nonlinear similar element technique, CPU+GPU computational parallelization with multitasking. The superiority of BOFSM is demonstrated through the comprehensive seismic damage analysis of two frame structures. From the results, three conclusion can be summarized as follows:

- (1) The contribution of this work is to propose a practical and highly-efficient modeling and simulation protocol for predicting damage in large-scale engineering structures subjected to seismic excitation. Seamless integration of BIM with octree discretization enables the key advantages of automation and flexibility in allowing users to make edits and modifications to the model. The presented in this paper alleviated the difficulty in integrating BIM with structural analysis and pre-preprocessing can be achieved in a timely manner (estimated to be dozens of times faster than conventional means).
- (2) Three techniques are recommended to optimize the analysis efficiency. Firstly, a coupled SBFEM-FEM strategy is suggested for enhancing the computational efficiency. In the strategy, FEM is employed to solve hexahedron isoparametric elements occupying more than 90% of the model while SBFEM is used to solve the polyhedron elements which comprised about 10% of the model. Secondly, a nonlinear similar element method for 3D problems is proposed for further improving solution speeds. Taking full advantage of characteristics of the octree discretization, more than 80% of the cube elements were processed economically.

Leveraging the similarity among differently sized elements (with same aspect ratios), the stiffness matrices  $K$ , mass matrices  $M$ , damping matrices  $C$  and the value in the Gaussian points  $K_i$ ,  $M_i$  and  $C_i$  of one unit cubic element are pre-computed once and stored in the memory. The data can be subsequently retrieved and scaled as necessary in each load step. Thirdly, CPU+GPU parallelization and multitasking were incorporated to accelerate the solving of equations, matrix operations, and disk read-write speeds. In this manner, approximately 40% computational time has been reduced.

- (3) The proposed method has strong versatility, practicality and robustness. It can be readily extended to perform detailed damage simulation for other complex engineering problems. The advantages of the method were demonstrated through an exemplary numerical simulation of a complex frame structure. We envision that the method can be extended to a broader range of applications, such as the simulation of urban catastrophes, seismic analysis of underground structures and the failure analysis of major civil engineering structures, all of which will be investigated in the future.

## Acknowledgments

This work was supported by National Key R&D Program of China (2017YFC0404904) and the [National Natural Science Foundation of China](#) (Grant nos. 51779034 and 51809034).

## References

- [1] Bazilevs Y, Calo VM, Cottrell JA, et al. Isogeometric analysis using T-splines. *Comput Methods Appl Mech Eng* 2010;199(5–8):229–63.
- [2] Succar B. Building information modelling framework: a research and delivery foundation for industry stakeholders. *Autom Constr* 2009;18(3):357–75.

- [3] Chi HL, Wang X, Jiao Y. BIM-enabled structural design: impacts and future developments in structural modelling, analysis and optimisation processes. *Arch Comput Methods Eng* 2015;22(1):135–51.
- [4] Olshanskii MA, Terekhov KM, Vassilevski YV. An octree-based solver for the incompressible Navier-Stokes equations with enhanced stability and low dissipation. *Comput Fluids* 2013;84:231–46.
- [5] Popinet S. An accurate adaptive solver for surface-tension-driven interfacial flows. *J Comput Phys* 2009;228(16):5838–66.
- [6] Fuster D, Bagué A, Boeck T, et al. Simulation of primary atomization with an octree adaptive mesh refinement and VOF method. *Int J Multiph Flow* 2009;35(6):550–65.
- [7] Korkut B, Li Z, Levin DA. 3-D simulation of ion thruster plumes using octree adaptive mesh refinement. *IEEE Trans Plasma Sci* 2015;43(5):1706–21.
- [8] Zou D, Chen K, Kong X, et al. An enhanced octree polyhedral scaled boundary finite element method and its applications in structure analysis. *Eng Anal Boundary Elem* 2017;84:87–107.
- [9] Liu Y, Saputra AA, Wang J, et al. Automatic polyhedral mesh generation and scaled boundary finite element analysis of STL models. *Comput Methods Appl Mech Eng* 2017;313:106–32.
- [10] Saputra A, Talebi H, Tran D, et al. Automatic image-based stress analysis by the scaled boundary finite element method. *Int J Numer Methods Eng* 2017;109(5):697–738.
- [11] Wolf JP, Song CM. Finite-element modelling of unbounded media. Chichester: Wiley; 1996.
- [12] Beskos DE. Boundary element methods in dynamic analysis. *Appl Mech Rev* 1987;40(1):1–23.
- [13] Beskos DE, Maier GE. Boundary element advances in solid mechanics. Springer; 2014.
- [14] Liu J, Lin G. A scaled boundary finite element method applied to electrostatic problems. *Eng Anal Boundary Elem* 2012;36(12):1721–32.
- [15] Liu J, Zhang PC, Lin G, et al. High order solutions for the magneto-electro-elastic plate with non-uniform materials. *Int J Mech Sci* 2016;115:532–51.
- [16] Ooi ET, Song C, Tin-Loi F. A scaled boundary polygon formulation for elasto-plastic analyses. *Comput Methods Appl Mech Eng* 2014;268:905–37.
- [17] Chen K, Zou D, Kong X, et al. A novel nonlinear solution for the polygon scaled boundary finite element method and its application to geotechnical structures. *Comput Geotech* 2017;82:201–10.
- [18] Chen K, Zou D, Kong X. A nonlinear approach for the three-dimensional polyhedron scaled boundary finite element method and its verification using Koyna gravity dam. *Soil Dyn Earthq Eng* 2017;96:1–12.
- [19] Goswami S, Becker W. Computation of 3-D stress singularities for multiple cracks and crack intersections by the scaled boundary finite element method. *Int J Fract* 2012;175(1):13–25.
- [20] Ooi ET, Shi MG, Song CM, et al. Dynamic crack propagation simulation with scaled boundary polygon elements and automatic remeshing technique. *Eng Fract Mech* 2013;106:1–21.
- [21] Ooi ET, Natarajan S, Song C, et al. Dynamic fracture simulations using the scaled boundary finite element method on hybrid polygon quadtree meshes. *Int J Impact Eng* 2016;90:154–64.
- [22] Saputra AA, Birk C, Song C. Computation of three-dimensional fracture parameters at interface cracks and notches by the scaled boundary finite element method. *Eng Fract Mech* 2015;148:213–42.
- [23] Lu S, Liu J, Lin G, et al. Time-domain analyses of the layered soil by the modified scaled boundary finite element method. *Struct Eng Mech* 2015;55(5):1055–86.
- [24] Birk C, Behnke R. A modified scaled boundary finite element method for three-dimensional dynamic soil-structure interaction in layered soil. *Int J Numer Methods Eng* 2012;89(3):371–402.
- [25] Lu S, Liu J, Lin G, et al. Modified scaled boundary finite element analysis of 3D steady-state heat conduction in anisotropic layered media. *Int J Heat Mass Transf* 2017;108:2462–71.
- [26] Lin G, Liu J, Li J, et al. A scaled boundary finite element approach for sloshing analysis of liquid storage tanks. *Eng Anal Boundary Elem* 2015;56:70–80.
- [27] Xu H, Zou D, Kong X, et al. A nonlinear analysis of dynamic interactions of CFRD-compressible reservoir system based on FEM-SBFEM. *Soil Dyn Earthq Eng* 2018;112:24–34.
- [28] Liu J, Lin G, Li J. Short-crested waves interaction with a concentric cylindrical structure with double-layered perforated walls. *Ocean Eng* 2012;40:76–90.
- [29] Gravenkamp H, Saputra AA, Song C, et al. Efficient wave propagation simulation on quadtree meshes using SBFEM with reduced modal basis. *Int J Numer Methods Eng* 2017;110(12):1119–41.
- [30] Chen D, Birk C, Song C, et al. A high-order approach for modelling transient wave propagation problems using the scaled boundary finite element method. *Int J Numer Methods Eng* 2014;97(13):937–59.
- [31] Li P, Liu J, Lin G, et al. A NURBS-based scaled boundary finite element method for the analysis of heat conduction problems with heat fluxes and temperatures on side-faces. *Int J Heat Mass Transf* 2017;113:764–79.
- [32] Xu H, Zou D, Kong X, et al. Study on the effects of hydrodynamic pressure on the dynamic stresses in slabs of high CFRD based on the scaled boundary finite-element method. *Soil Dyn Earthq Eng* 2016;88:223–36.
- [33] Xu H, Zou D, Kong X, et al. Error study of Westergaard's approximation in seismic analysis of high concrete-faced rockfill dams based on SBFEM. *Soil Dyn Earthq Eng* 2017;94:88–91.
- [34] Zou DG, Teng XW, Chen K, et al. An extended polygon scaled boundary finite element method for the nonlinear dynamic analysis of saturated soil. *Eng Anal Boundary Elem* 2018;91:150–61.
- [35] Song C, Ooi ET, Pramod ALN, et al. A novel error indicator and an adaptive refinement technique using the scaled boundary finite element method. *Eng Anal Boundary Elem* 2018;94:10–24.
- [36] Natarajan S, Ooi ET, Saputra A, et al. A scaled boundary finite element formulation over arbitrary faceted star convex polyhedra. *Eng Anal Boundary Elem* 2017;80:218–29.
- [37] Gravenkamp H, Natarajan S. Scaled boundary polygons for linear elastodynamics. *Comput Methods Appl Mech Eng* 2018;333:238–56.
- [38] Guo H, Ooi ET, Saputra AA, et al. A quadtree-polygon-based scaled boundary finite element method for image-based mesoscale fracture modelling in concrete. *Eng Fract Mech* 2019;211:420–41.
- [39] Chen X, Luo T, Ooi ET, et al. A quadtree-polygon-based scaled boundary finite element method for crack propagation modeling in functionally graded materials. *Theor Appl Fract Mech* 2018;94:120–33.
- [40] Talebi H, Saputra A, Song C. Stress analysis of 3D complex geometries using the scaled boundary polyhedral finite elements. *Comput Mech* 2016;58(4):697–715.
- [41] Saputra AA, Birk C, Song C. Computation of three-dimensional fracture parameters at interface cracks and notches by the scaled boundary finite element method. *Eng Fract Mech* 2015;148:213–42.
- [42] Zhang Z, Dissanayake D, Saputra A, et al. Three-dimensional damage analysis by the scaled boundary finite element method. *Comput Struct* 2018;206:1–17.
- [43] Zhang Z, Liu Y, Dissanayake DD, et al. Nonlocal damage modelling by the scaled boundary finite element method. *Eng Anal Boundary Elem* 2019;99:29–45.
- [44] Chen K, Zou D, Kong X, et al. Global concurrent cross-scale nonlinear analysis approach of complex CFRD systems considering dynamic impervious panel-rockfill material-foundation interactions. *Soil Dyn Earthq Eng* 2018;114:51–68.
- [45] Eastman C, Teicholz P, Sacks R, Liston K. BIM handbook: a guide to building information modeling for owners, managers, designers, engineers and contractors. Wiley; 2011.
- [46] Sacks R, Barak R. Impact of three-dimensional parametric modeling of buildings on productivity in structural engineering practice. *Autom Constr* 2008;17(4):439–49.
- [47] Azhar S. Building information modeling (BIM): trends, benefits, risks and challenges for the AEC industry. *Leadersh Manag Eng* 2011;11:241–52.
- [48] . BIM for facility managers. BIM for facility managers. Teicholz PM, editor. Hoboken, N.J.: John Wiley & Sons; 2013.
- [49] Krygiel E, Nies B, Krygiel E, Nies B. Green BIM: successful sustainable design with building information modeling. Indianapolis, Ind.: Wiley; 2008.
- [50] Peterson F, Hartmann T, Fruchter R, Fischer M. Teaching construction project management with BIM support: experience and lessons learned. *Autom Constr* 2011;20(2):115–25.
- [51] <https://www.autodesk.com/products/revit/overview>, 2019.
- [52] <https://www.autodesk.com/products/revit/structure#>, 2019.
- [53] Rashid MM, Selimotic M. A three-dimensional finite element method with arbitrary polyhedral elements. *Int J Numer Methods Eng* 2006;67(2):226–52.
- [54] Wicke M, Botsch M, Gross M. A finite element method on convex polyhedra. *Comput Graph Forum, Blackwell Publishing Ltd*. 2007;26(3):355–64.
- [55] Martin S, Kaufmann P, Botsch M, et al. Polyhedral finite elements using harmonic basis functions. *Comput Graph Forum, Blackwell Publishing Ltd*. 2008;27(5):1521–9.
- [56] Bishop JE. Simulating the pervasive fracture of materials and structures using randomly close packed Voronoi tessellations. *Comput Mech* 2009;44(4):455–71.
- [57] Natarajan S, Bordas S, Ooi ET. Virtual and smoothed finite elements: a connection and its application to polygonal/polyhedral finite element methods. *Int J Numer Methods Eng* 2015;104(13):1173–99.
- [58] Chen K, Zou D, Kong X, et al. An efficient nonlinear octree SBFEM and its application to complicated geotechnical structures. *Comput Geotech* 2018;96:226–45.
- [59] Lee J, Fenves GL. Plastic-damage model for cyclic loading of concrete structures. *J Eng Mech ASCE* 1998;124(8):892–900.
- [60] Lee J. Theory and implementation of plastic-damage model for concrete structures under cyclic and dynamic loading Ph.D. Thesis. Berkeley: University of California; 1996.
- [61] Lubliner J, Oliver J, Oller S, Onate E. A plastic-damage model for concrete. *Int J Solid Struct* 1989;25(3):299–326.
- [62] Ooi ET, Man H, Natarajan S, et al. Adaptation of quadtree meshes in the scaled boundary finite element method for crack propagation modelling. *Eng Fract Mech* 2015;144:101–17.
- [63] Zou DG, Kong XJ, Xu B. User manual for geotechnical dynamic nonlinear analysis, Dalian: Institute of Earthquake Engineering, Dalian University of Technology; 2005. (in Chinese).
- [64] Kong XJ, Zhou Y, Zou DG, et al. Numerical analysis of dislocations of the face slabs of the Zipingpu concrete faced rockfill dam during the Wenchuan earthquake. *Earthq Eng Vib* 2011;10(4):581–9.
- [65] Xu B, Zou DG, Liu HB. Three-dimensional simulation of the construction process of the Zipingpu concrete face rockfill dam based on a generalized plasticity model. *Comput Geotech* 2012;43:143–54.
- [66] Zou DG, Xu B, Kong XJ, et al. Numerical simulation of the seismic response of the Zipingpu concrete face rockfill dam during the Wenchuan earthquake based on a generalized plasticity model. *Comput Geotech* 2013;49:111–22.
- [67] Zou DG, Zhou Y, Ling HI, et al. Dislocation of face-slabs of Zipingpu concrete face rockfill dam during Wenchuan earthquake. *J Earthq Tsunami* 2012;6(2):1–17.
- [68] Xu B, Zhou Y, Zou DG. Numerical simulation on slabs dislocation of Zipingpu concrete faced rockfill dam during the Wenchuan earthquake based on a generalized plasticity model. *Sci World J* 2014;7(1):1–5.